◁AIAA.

AIAA 99-0813
Nonparallel Stability Analysis of Compressible
Boundary Layer using 3-D PSE

S. H. Hu and Xiaolin Zhong
University of California, Los Angeles
Los Angeles, CA

37th Aerospace Sciences
Meeting & Exhibit
January 11–14, 1999 / Reno, NV

Nonparallel Stability Analysis of Compressible Boundary Layer using 3-D PSE

Sean Hu *and Xiaolin Zhong [†]

University of California, Los Angeles, California 90095

Abstract

The receptivity, stability and transition mechanisms of hypersonic flows over 3-D bodies have been the focus of recent research efforts. 2-D and 3-D DNS (Direct Numerical Simulation) have been used as a primary tool in attacking the problems. However, to fully address the problems, less costly methods are desirable to provide independent checks and theoretical interpretations of the numerical results. 3-D PSE (Parabolized Stability Equations), a 3-D extension of the 2-D linear PSE, derived from the full compressible Navier-Stokes disturbance equations in generalized coordinates, have been developed as a cost effective alternative to DNS in solving the problems. Specifically, 3-D PSE intend to account for spanwise variations of basic flow as well as the wavenumbers and shape functions of the disturbances which are ignored in 2-D PSE. Along with 3-D DNS to provide the receptivity solutions, 3-D PSE may serve as a very practical tool in understanding the 3-D stability and transition mechanisms for compressible flows. The formulations and numerical methodology are presented for 2-D and 3-D PSE. At the testing stage, 2-D and 3-D linear PSE are validated with previous 2-D linear PSE results for supersonic flows over flat plate.

1   Introduction

The understanding of the stability and transition mechanisms of high-speed flows are critical to the accurate calculations of aerodynamic forces and heatings to supersonic and hypersonic vehicles. Current understanding of the laminar-turbulent transition in compressible boundary layers comes mainly from the parallel linear stability theory [1-4]. Mack [2] did extensive work on the linear stability of 2-D and 3-D supersonic boundary layers and shear flows. One of the most important contributions by Mack to the compressible linear theory is that he discovered a new family of higher

---

*Graduate Student,AIAA member

[†]Associate Professor, Mechanical and Aerospace Engineering Department, Member AIAA

modes at supersonic speeds. He showed that, for compressible boundary layer stability, the lowest-frequency two-dimensional second mode (Mack mode) is the most unstable one for Mach number greater than about 4.

The linear stability theory (LST) provides many insights on the stability properties of hypersonic boundary layers. However, it neglects non-parallel effects of the boundary layer and confines the stability analysis to local stations of the boundary layer. For hypersonic flow over 3-D bodies, such as elliptical cones, basic flow changes in both streamwise, and spanwise direction and the transition process is indeed a 3-D process. Moreover, the effects of the bow shocks have to be taken into account when the bow shocks are close to the body surfaces. The traditional linear stability theory and the e^N method for transition prediction do not account for these effects. The remedies in these situations may be the direct numerical simulations (DNS), the Parabolized Stability Equations (PSE) methods.

Recently, DNS of hypersonic flows over 2-D and 3-D blunt bodies including the effects of boundary layers and shock layers were conducted by Zhong [5] [6] [7] who studied the generation of instability waves due to freestream acoustic disturbances for 2-D and 3-D hypersonic flows by numerically solving full Navier-Stokes equations using a new explicit fifth-order shock fitting upwind scheme. Better understanding of the stability characteristics of the hypersonic parabolic body flow can be achieved if the overall wave phenomena from DNS can be decomposed into linear and nonlinear parts, and the effects of the shock wave, and the 3-D basic flow can be identified. Due to the high computational demand of DNS, especially for 3-D DNS, more efficient numerical methods are desirable. PSE, which were originally developed by Herbert and Bertolotti. [8-11] are certainly a good candidate for that purpose. In LST, in a Cartesian coordinate system, where (x, y, z) represent the streamwise, wall normal and spanwise directions respectively, the disturbances by the normal mode assumption are

$$q'(x, y, z, t) = \hat{q}(y) exp[i(\alpha x + \beta z - \omega t)]. \quad (1)$$

While in PSE, the disturbances are expressed as

$$q'(x,y,z,t) = \hat{q}(x,y)exp[\int_{x_0}^{x} \alpha d\xi + i\beta z - i\omega t], \quad (2)$$

which subject to a constraint imposed to ensure the slow change in shape function $\hat{q}(x,y)$.

The traditional difficulty in studying transition has been the streamwise ellipticity of the equations and the outflow boundary conditions to the passage of disturbances. To bypass the traditional difficulty, Herbert and coworkers parabolized the governing equations by eliminating the streamwise derivatives that are higher than the first order utilizing the above form (Eq. 2) for disturbances. Spatial evolution of disturbances is then computed by an efficient space marching algorithm. Despite the parabolization, PSE exhibit weak ellipticity. Efforts have also been made to study the mathematical nature of PSE. The related papers include Haj-Hariri [12], Li and Malik [13] among with other papers. With careful treatment of numerical procedure, PSE are capable of including the nonparallel and nonlinear effects neglected by the linear parallel theory. PSE have been embraced by many authors since their genesis. Chang *et al.* [14], and subsequently Airiau *et al.* [15] have all utilized PSE as tools for stability analysis. The PSE have been successfully applied to many subsonic and supersonic boundary layers for both linear and nonlinear stabilities. It has also been extended to study the cross flow instabilities over quasi-2-D boundary layers. [11] [13] Chang and Malik [16,17] also investigated the linear and nonlinear stability of compressible growing boundary layers using PSE. Recently, Chang, Vinh and Malik [18] used PSE to study the linear stability of the reacting flows in hypersonic boundary layers. Three gas models, perfect gas, chemical equilibrium and non-equilibrium, were considered. Rankine-Hugoniout shock conditions were also applied at the shock.

The latest developments in PSE are the extension of PSE to truely 3-D flows. Herbert [19,20] discussed the progress in applying the PSE to 3-D applications. Previously, PSE were only used to solve the stability problems of 2-D and quasi-2-D boundary layers where the spanwise variation of the basic flow is ignored. Herbert discussed the extension of 2-D PSE to PSE/3D where the disturbances grow both along the streamwise and spanwise directions. The objective of this paper is to develop and demonstrate a modified 3-D PSE to solve for the stability of hypersonic flow over 3-D bodies, specifically 3-D elliptical cones, with nonparallel, 3-D and shock effects to compare with the DNS solutions. The body geometry and the basic flow solutions of a Mach 15 flow over an elliptical blunt cone

are shown in Fig.1. Several modifications are needed for PSE to solve this types of problems. The presence of the bow shock over the 3-D body may require special treatment in PSE. Previously, shock jump conditions have been implemented for the linear stability analysis of 2-D parabolic bodies [21], it is convenient to enforce the same conditions for PSE. The spanwise variation of basic flow is clearly seen f rom the spanwise cross section Mach number contour. What is also evident from the primary unsteady DNS results shown in Fig.4 is the spanwise dependence of the disturbances. The situations differ from the cases described by Herbert [19] [11] in that the disturbances in the spanwise direction can be assumed to be periodic. These facts lead to an extension from 2-D PSE with the following features. The disturbances in the transformed coordinate system, where ξ, η, ζ are streamwise, normal, and spanwise direction respectively, are expressed as:

$$q'(\xi,\eta,\zeta,\tau) = \hat{q}(\xi,\eta,\zeta)exp[\int_{\xi_0}^{\xi} \alpha d\xi' - i\omega\tau], \quad (3)$$

where the determination of the 3-D dependence of $\hat{q} = \hat{q}(\xi,\eta,\zeta)$, and the 2-D dependence of $\alpha = \alpha(\xi,\zeta)$ demand the 2-D PSE procedure to be modified. The modifications in the numerical methods and procedures necessary for 3-D PSE from 2-D PSE are the focuses of the paper. The demonstrations of 2-D PSE and 3-D PSE methods are only carried out for compressible boundary layers over flat plate at this stage.

2 Governing Equations

Both the compressible linear stability equations (LST) and the parabolic stability equations (PSE) originate from the compressible Navier-Stokes equations. The gas is assumed to be perfect Newtonian gas. The three dimensional Navier-Stokes equations in Cartesian coordinates (x^*,y^*,z^*), where * denotes dimensional quantities, are.

$$\rho^* [\frac{\partial u^*}{\partial t^*} + u^* \cdot \nabla u^*] = -\nabla p^* + \nabla \cdot [\lambda^*(\nabla \cdot u^*) I + \mu^*(\nabla u^* + \nabla u^{*tr})], \quad (4)$$

$$\frac{\partial \rho^*}{\partial t^*} + \nabla \cdot (\rho^* u^*) = 0, \quad (5)$$

$$\rho^* c_p^* [\frac{\partial T^*}{\partial t^*} + u^* \cdot \nabla T^*] = \nabla \cdot (k^* \nabla T^*) + \frac{\partial p^*}{\partial t^*} + u^* \cdot \nabla u^* + \Phi^*, \quad (6)$$

$$p^* = \rho^* R^* T^*, \quad (7)$$

2

where $\mathbf{u}^*$ is the velocity vector, ρ^* is the density, p^* is the pressure, T^* is the temperature, R^* is the gas constant, c_p^* is the specific heat at constant pressure, k^* is the thermal conductivity, μ^* is the first coefficient of viscosity, and λ^* is the second coefficient of viscosity. The viscous dissipation function, Φ^*, is given as

$$\Phi^* = \lambda^*(\nabla \cdot \mathbf{u}^*)^2 + \frac{\mu^*}{2}[\nabla \mathbf{u}^* + \nabla \mathbf{u}^{*tr}]^2 . \quad (8)$$

In the derivation of linear disturbance equations, we closely followed Malik's [22] formulation in Cartesian coordinates. The flow variables and equations are nondimensionalized as follows: velocity by U_∞^*, density by ρ_∞^*, pressure by $\rho_\infty^* U_\infty^{*2}$, length scales by a fixed $\delta = \sqrt{\nu^* x^* U_\infty^*}$, and time scale by δ^*/U_∞^* where x^* denotes distance from the leading edge. For PSE formulations in particular, $\delta = \delta(x_0^*)$ is used where x_0^* is the starting point in the streamwise direction for the marching procedure. Instantaneous flow variables are represented as the sums of mean values and fluctuations, i.e.

$$
\begin{aligned}
u &= \overline{U}(x,y,z) + \tilde{u}(x,y,z,t) \\
v &= \overline{V}(x,y,z) + \tilde{v}(x,y,z,t) \\
w &= \overline{W}(x,y,z) + \tilde{w}(x,y,z,t) \\
p &= \overline{P}(x,y,z) + \tilde{p}(x,y,z,t) \\
T &= \overline{T}(x,y,z) + \tilde{T}(x,y,z,t)
\end{aligned}
\quad (9)
$$

The disturbance equations are recast using a completely general transformation of the form:

$$
\begin{aligned}
\xi &= \xi(x,y,z) \\
\eta &= \eta(x,y,z) \quad , \\
\zeta &= \zeta(x,y,z)
\end{aligned}
\quad (10)
$$

where ξ, η, ζ are streamwise, normal, and spanwise direction respectively.

Finally we obtain the disturbance equations in the following form,

$$
\begin{aligned}
&A\tilde{q} + B \frac{\partial \tilde{q}}{\partial \tau} + C \frac{\partial \tilde{q}}{\partial \xi} + D \frac{\partial \tilde{q}}{\partial \eta} \\
&+E \frac{\partial \tilde{q}}{\partial \zeta} + F \frac{\partial^2 \tilde{q}}{\partial \xi^2} + G \frac{\partial^2 \tilde{q}}{\partial \eta^2} + H \frac{\partial^2 \tilde{q}}{\partial \zeta^2} \\
&+I \frac{\partial^2 \tilde{q}}{\partial \xi \partial \eta} + J \frac{\partial^2 \tilde{q}}{\partial \eta \partial \zeta} + L \frac{\partial^2 \tilde{q}}{\partial \xi \partial \zeta} = 0
\end{aligned}
\quad (11)
$$

where,

$$
\tilde{q} = \begin{bmatrix} \tilde{u}(\xi,\eta,\zeta,\tau) \\ \tilde{v}(\xi,\eta,\zeta,\tau) \\ \tilde{p}(\xi,\eta,\zeta,\tau) \\ \tilde{T}(\xi,\eta,\zeta,\tau) \\ \tilde{w}(\xi,\eta,\zeta,\tau) \end{bmatrix} .
\quad (12)
$$

2.1 2-D PSE and 3-D PSE formulation

To derive the 2-D PSE formulation, the disturbance is expressed in the following form:

$$\tilde{q} = \hat{q}(\xi,\eta)exp[\int_{\xi_0}^{\xi} \alpha d\xi + i\beta\zeta - i\omega\tau)] \quad , \quad (13)$$

or

$$\tilde{q} = \psi A \quad , \quad (14)$$

where $\alpha = \alpha(\xi)$ only for 2-D PSE, and $A = exp[\int_{\xi_0}^{\xi} \alpha d\xi + i\beta\zeta - i\omega\tau)]$. Substituting the PSE assumptions,

$$
\begin{aligned}
\tilde{q}_\xi &= \psi_\xi A + \psi i\alpha A, \\
\tilde{q}_{\xi\xi} &= i\alpha_\xi \psi A + 2i\psi_\xi \alpha A - \psi\alpha^2 A,
\end{aligned}
\quad (15)
$$

and ignoring the $O(1/R^2)$ terms, Eqs 11 can be rewritten as the following:

$$\hat{A}\hat{q} + \hat{B}\hat{q}_\xi + \hat{C}\hat{q}_\eta + \hat{D}\hat{q}_{\eta\eta} = 0, \quad (16)$$

where $\hat{A}, \hat{B}, \hat{C}, \hat{D}$ are operaters acting in η direction. β is assumed to be real and is contained in $\hat{A}, \hat{B}, \hat{C}$ along with the basic flow terms. This formulation is consistent with the well accepted 2-D PSE formulation.

For problems such as compressible flow over 3-D bodies with elliptical cross sections, one may assume disturbances only grow streamwise. Also β may vary in the streamwise direction. The basic flow is 3-D. More importantly, the disturbances are also 3-D. So the 2-D PSE assumptions may not be suitable for stability analysis. However, 3-D stability analysis is still in its infancy. Here a 3-D PSE formulation is proposed to fully account for the 3-D nature of basic flow. In this 3-D PSE formulation, the local shape function $\hat{q}$ is assumed to be 2-D, that is $\hat{q} = \hat{q}(\eta,\zeta)$. Accordingly, the normal wave assumption is relaxed in the spanwise direction ζ, which leads to

$$\tilde{q} = \hat{q}(\xi,\eta,\zeta)exp[\int_{\xi_0}^{\xi} \alpha d\xi' - i\omega\tau)] \quad . \quad (17)$$

Early DNS results for the hypersonic flow over 3-D bodies with elliptical cross sections show that the wavenumbers of the disturbances α vary in both ξ, and ζ directions, that is $\alpha = \alpha(\xi,\zeta)$, see Fig.4. This fact entails determination of the spanwise dependent α in the

marching procedure, which is achieved with a special normalization procedure extended from the standard 2-D PSE normalization procedure. The normalization procedures are discussed in the next section. Here, we present the formulation of 3-D PSE as follows:

$$
\begin{aligned}
& \hat{A}\hat{q} + \hat{B}\hat{q}_\xi + \hat{C}\hat{q}_\eta + \hat{D}\hat{q}_{\eta\eta} \\
& +\hat{E}\hat{q}_\zeta + \hat{F}\hat{q}_{\zeta\zeta} + \hat{G}\hat{q}_{\eta\zeta} = 0
\end{aligned}
\tag{18}
$$

where the spanwise wavenumber β in the 2-D PSE formulation is replaced by spanwise (ζ) direction derivatives. The coefficient matrices are defined over the coefficient matrices in Eq.11 as:

$$
\begin{aligned}
\hat{A} &= A - i\omega B + i\alpha C + i\alpha_\xi F \\
&\quad +i\alpha_\zeta L - \alpha^2 F, \\
\hat{B} &= C + 2i\alpha F, \\
\hat{C} &= D + i\alpha I \\
\hat{D} &= G \\
\hat{E} &= E + i\alpha L \\
\hat{F} &= H \\
\hat{G} &= J
\end{aligned}
\tag{19}
$$

The Neuman conditions on pressure are enforced as

$$
\left. \frac{\partial p}{\partial y} \right|_{y=0} = a, \quad \left. \frac{\partial p}{\partial y} \right|_{y=1} = b
\tag{20}
$$

where a and b are evaluated at the two boundaries using the normal momentum equations. Dirichlet boundary conditions are used for the flat plate boundary layer case both at the wall and the free stream:

$$
\hat{u} = \hat{v} = \hat{w} = \hat{T} = 0 \ at \ y = 0
\tag{21}
$$

$$
\hat{u} = \hat{v} = \hat{w} = \hat{T} = 0 \ at \ y \to \infty
\tag{22}
$$

When the shock is present, in addition to the above formulation, the Rankine-Hugoniot shock jump conditions derived early [21] replace the free stream boundary conditions.

Having laid out the formulations for 2-D and 3-D PSE, the numerical methods used for solving the equations are discussed in the following section.

3   Numerical Methods

Solving 2-D PSE entails numerical discritization in both the streamwise and wall normal directions. Typical discritization method in the streamwise direction is the implicit backward Euler method. In the wall normal direction, the use of spectral collocation methods and fourth order finite different methods (4FDM) are both reported. The determining factor in choosing the streamwise schemes is stability. In the wall normal direction, schemes with the grid distributions suitable at certain Mach number are chosen, because of the outward moving tendency of the boundary layer as Mach number increases. For practical reasons, current PSE also use the implicit backward Euler in the streamwise direction. A spectral collocation method with an algebraic stretching function is used for Mach number less than 4.5 cases, whereas 4FDM is used for Mach 4.5 cases. 3-D PSE require discritization in spanwise direction also. When the number of grid points is limited and simple wave solutions are expected in the spanwise direction, a Fourier collocation method is a good candidate.

3.1   Spectral collocation method

The discretization formulas using the spectral collocation method can be found in Malik [22] and are given below for completeness.

The Nth-order Chebyshev polynomials T_N are defined on the interval $j \in [-1, 1]$. The collocation points ξ_j, which are the extrema of T_N, are

$$
\xi_j = cos\frac{\pi j}{N}, \quad j = 0, 1, \ldots, N.
\tag{23}
$$

In order to apply the spectral collocation method, an interpolant polynomial is constructed for the dependent variables in terms of their values at the collocation points. An Nth-order polynomial is

$$
\phi(\xi) = \sum_{k=0}^{N} \lambda_k(\xi)\phi(\xi_k)
\tag{24}
$$

where the interpolant $\lambda_k(\xi)$ for the Chebyshev scheme is

$$
\lambda_k(\xi) = \left(\frac{1 - \xi^2}{\xi - \xi_k}\right)\frac{T_N(\xi)}{N^2 c_k}(-1)^{(k+1)}
\tag{25}
$$

4

where $c_0 = c_N = 2$, and $c_k = 1$, $0 < k < N$.

The first derivative of $\phi(\xi)$ may be written as

$$\left.\frac{d\phi}{d\xi}\right|_j = \sum_{k=0}^{N} E_{jk}\phi_k \qquad (26)$$

where E_{jk} are the elements of the derivative matrix defined as:

$$E_{jk} = \frac{c_j}{c_k}\frac{(-1)^{k+j}}{\xi_j + \xi_k}, \qquad j \neq k \qquad (27)$$

$$E_{jj} = \frac{\xi_j}{2(1 - \xi_j^2)}, \qquad (28)$$

$$E_{00} = -E_{NN} = \frac{2N^2 + 1}{6}. \qquad (29)$$

The transformation between physical and computational domains is

$$y = a\frac{1 + \xi}{b - \xi}, \qquad (30)$$

where

$$b = \frac{1 + 2a}{y_{max}}, \quad a = \frac{y_i y_{max}}{y_{max} - 2y_i}. \qquad (31)$$

Half the grid points are located between y_i and the wall.

Therefore the scaling factor for the transformation between physical domain y and computational domain ξ is given as

$$S_j = \left.\frac{\partial \xi}{\partial y}\right|_j ; \qquad j = 0, 1, ..., N \qquad (32)$$

then the first derivative matrix F in the physical domain may be written as

$$F_{jk} = S_j E_{jk} \qquad (33)$$

and the second derivative matrix G_{jk} is

$$G_{jk} = F_{jm}F_{mk} \qquad (34)$$

The stretching function for this collocation method is the algebraic stretching where y_i is normally assigned to be the displacement thickness of the boundary layer.

3.2 Fourth-order finite-difference method

In implementing the fourth-order finite-difference method, we use a non-staggered grid. One-sided difference formulas which do not involve the wall points are used to approximate the first derivative of $\hat{p}$. The derivatives to be represented here are assumed to be $D\phi/dy, D^2\phi/dy^2$. The fourth-order finite-difference formulas at a grid point j, where j is from 1 to $N + 1$, are the following.
For j from 3 to $N - 1$,

$$D^2\phi_j = \frac{1}{12\Delta y^2}(-\phi_{j+2} + 16\phi_{j+1} - 30\phi_j + 16\phi_{j-1} - \phi_{j-2}), \qquad (35)$$

$$D\phi_j = \frac{1}{12(\Delta y)}(-\phi_{j+2} + 8\phi_{j+1} - 8\phi_{j-1} + \phi_{j-2}). \qquad (36)$$

For $j = 2$:

$$D^2\phi_j = \frac{1}{12(\Delta y)^2}(10\phi_{j-1} - 15\phi_j - 4\phi_{j+1} + 14\phi_{j+2} - 6\phi_{j+3} + \phi_{j+4}), \qquad (37)$$

$$D\phi_j = \frac{1}{12(\Delta y)}(-3\phi_{j-1} - 10\phi_j + 18\phi_{j+1} - 6\phi_{j+2} + \phi_{j+3}). \qquad (38)$$

For $j = N$:

$$D^2\phi_j = \frac{1}{12(\Delta y)^2}(\phi_{j-4} - 6\phi_{j-3} + 14\phi_{j-2} - 4\phi_{j-1} - 15\phi_j + 10\phi_{j+1}), \qquad (39)$$

$$D\phi_j = \frac{1}{12(\Delta y)}(-\phi_{j-3} + 6\phi_{j-1} - 18\phi_{j-1} + 10\phi_j + 3\phi_{j+1}). \qquad (40)$$

The first derivative of $\hat{p}$ near the wall are given below.
For $j = 2$:

$$D\phi_j = \frac{1}{12(\Delta y)}(-25\phi_j + 48\phi_{j+1} - 36\phi_{j+2} + 16\phi_{j+3} - 3\phi_{j+4}). \qquad (41)$$

For $j = 3$:

$$D\phi_j = \frac{1}{12(\Delta y)}(-3\phi_{j-1} - 10\phi_j + 18\phi_{j+1} - 6\phi_{j+2} + \phi_{j+3}). \qquad (42)$$

5

For $j = N$:

$$D\phi_j = \frac{1}{12(\Delta y)}(3\phi_{j-4} - 16\phi_{j-3} + 36\phi_{j-2} - 48\phi_{j-1} + 25\phi_j). \tag{43}$$

For $j = N - 1$:

$$D\phi_j = \frac{1}{12(\Delta y)}(-\phi_{j-3} + 6\phi_{j-2} - 18\phi_{j-1} + 10\phi_j + 3\phi_{j+1}). \tag{44}$$

The stretching functions used for the 4FDM method vary with Mach number. Instead of clustering points close to the wall as in the low Mach number cases, at Mach 4.5, a stretching function that clusters grid points near an interior point is used for satisfactory results.

3.3 Fourier collocation method

The Fourier collocation method is used in the spanwise direction for the test case where Cartesian coordinates (x, y, z) are used. The spanwise grid distribution is uniform with

$$z_j = \frac{j}{N}, \ z \in [0, L], \ L = 1, \tag{45}$$

where N is the number of grid points in z direction. Note here that the spanwise direction is scaled with the spanwise wave length. The Fourier collocation differentiation matrices are:

$$\frac{\partial \phi}{\partial z}|_l = d^1_{lj}\phi_j$$
$$\frac{\partial^2 \phi}{\partial z^2}|_l = d^1_{lm}d^1_{mj}\phi_j \tag{46}$$

where d^1_{lj} may be evaluated in closed form:

$$d^1_{lj} = \frac{\pi}{L}(-1)^{l+j}cot(\frac{\pi(l-j)}{N}), \ l \neq \textsc{j},$$
$$d^1_{lj} = 0, \ l = j. \tag{47}$$

3.4 3-D PSE formulation

For the simple test case of flat plate boundary layer with periodic solutions in the spanwise direction, accurate results can be achieved with very few grid points by using the Fourier collocation method. The use of the Fourier collocation differentiation in the spanwise direction entails a different scale in the spanwise direction. When simple wave solutions are expected in

the spanwise direction, the grid points are uniformly distributed in ζ. A natural choice of scale in this situation is thus the wave length λ_ζ. Thus the rescaled PSE equations are:

$$\hat{A}\hat{q} + \hat{B}\hat{q}_\xi + \hat{C}\hat{q}_\eta + \hat{D}\hat{q}_{\eta\eta} + \frac{\hat{E}}{\lambda_\zeta}\hat{q}_\zeta + \frac{\hat{F}}{\lambda_\zeta^2}\hat{q}_{\zeta\zeta} + \frac{\hat{G}}{\lambda_\zeta}\hat{q}_{\eta\zeta} = 0. \tag{48}$$

A major difference between 2-D and 3-D PSE is that, in 3-D PSE, local shape functions $\hat{q}$ are 2-D and are solved simultaneously. The local 2-D shape functions are also used to update the local wavenumbers α that vary in the spanwise direction.

3.5 2-D and 3-D PSE procedures

Both 2-D and 3-D PSE formulations can be rewritten in a simple format. Using a simple first order discritization scheme in the streamwise direction gives the following equation system to be solved at streamwise location $i+1$ given the solutions at the previous streamwise location i and the basic flow:

$$M_1\tilde{q} + M_2\frac{\tilde{q}_{j+1} - \tilde{q}_j}{\Delta x} = 0. \tag{49}$$

The computational cost in the eventural complex matrix inversion to obtain $\hat{q}$ increases proportionally with the grid numbers used in the spanwise direction, N_ζ. For 2-D PSE, the rank of the square complex matrix to be inversed is N_η, whereas for 3-D PSE, $N_\eta N_\zeta$.

An iterative procedure starts with assuming $\alpha_{i+1} = \alpha_i$, the following steps follow:

1. Solve for $\hat{q}_{i+1}$ while evaluating matrices M_1, M_2 at $j + 1$ using implicit backward Euler scheme.

2. Update α_{i+1} based on the new $\hat{q}_{i+1}, \hat{q}_i$ and some choice of normalization schemes.

3. Check if $\alpha^N_{i+1} - \alpha^O_{i+1} < \epsilon$. If yes, $i = i + 1$. If no, go back to step 1.

This procedure is repeated until the whole domain is traversed. Note here that $\alpha = \alpha(\xi)$ for the 2-D PSE, and $\alpha = \alpha(\xi, \eta)$ for the 3-D PSE. For the 2-D PSE, two formulas, namely,

$$\alpha^N = \alpha^O - i\frac{1}{\hat{u}_m}\frac{d\hat{u}_m}{d\xi} \tag{50}$$

where $\hat{u}_m$ may be the maximum streamwise disturbance in the wall normal direction at a fixed streamwise location,

$$\alpha^N = \alpha^O - i\frac{1}{E}\int_0^\infty \bar{\rho}(\hat{u}^\dagger\frac{\partial\hat{u}}{\partial\xi}+\hat{v}^\dagger\frac{\partial\hat{v}}{\partial\xi}+\hat{w}^\dagger\frac{\partial\hat{w}}{\partial\xi})d\eta \quad (51)$$

where $\dagger$ denote complex conjugates and E is given as

$$E = \int_0^\infty \bar{\rho}(|\hat{u}|^2 + |\hat{v}|^2 + |\hat{w}|^2)d\eta \quad (52)$$

which is independent of the wall normal coordinate. These two normalization schemes are referred to later in the paper as u and E normalizations respectively.

For 3-D PSE, the local wavenumbers α vary with ζ. Both u and E normalizations have to be extended for the ζ dependency. The u and E normalization formulas are modified, respectively, to be:

$$\alpha^N[k] = \alpha^O[k] - i\frac{1}{\hat{u}_m[k]}\frac{d\hat{u}_m[k]}{d\xi}, \quad (53)$$

$$\alpha^N[k] = \alpha^O[k] - i\frac{1}{E[k]}\int_0^\infty \bar{\rho}[k]$$
$$(\hat{u}^\dagger[k]\frac{\partial\hat{u}[k]}{\partial\xi} + \hat{v}^\dagger[k]\frac{\partial\hat{v}[k]}{\partial\xi} + \hat{w}^\dagger[k]\frac{\partial\hat{w}[k]}{\partial\xi})d\eta, \quad (54)$$

where k is the index for the spanwise grid points. Since at a fixed streamwise location ξ, there is one α_k corresponding to one spanwise location k, the extended normalzation procedure updates $\alpha[k]$ at each spanwise grid points before next iteration. The converged shape function satisfies the normalization condition at all spanwise locations and thus all $\alpha[k]$, $k \in [1, N_\zeta]$ are updated. This procedure allows the variation of wavenumbers in the spanwise direction which is observed in the early DNS results for the hypersonic elliptical cone case.

3.6 Initial conditions

The initial conditions for 2-D PSE come from either the nonparallel linear stability solutions or an iterative procedure solving the first order Taylor series expansions of the parallel linear stability results. The details of the latter method can be found in [8]. For 3-D PSE, the initial conditions may be obtained by extending the linear stability solutions to 3-D. Perhaps a better way for 3-D PSE is to use the DNS receptivity results which embodies both the receptivity mechanism near the leading edge and the 3-D nature of the basic flow and disturbance for the initial conditions.

Table 1: Effects of marching step size. $R_0 = 480, R = 963.7$

	α_i	difference
$\Delta x = 10$	$-0.27225e - 3$	-
$\Delta x = 20$	$-0.27449e - 3$	0.8%
$\Delta x = 40$	$-0.27890e - 3$	2.0%

Table 2: Effects of wall normal grid points. $R_0 = 400, R = 774.3$

	α_i	difference
$N_y = 121$	$-0.12906e - 2$	-
$N_y = 61$	$-0.12809e - 3$	0.7%

4 Code Validation and Result Discussion

The linear PSE results for compressible flat plate boundary layer are presented along with previously published results for validation purposes. Since the 3-D PSE code has been developed only recently, it has not been put to test against the DNS simulations due to the time constrain. For all the results presented, the computational field is scaled with δ_0 (except for the spanwise direction in the 3-D PSE cases), the boundary layer thickness at the starting point R_0. Other constants used throughout include $y_{max} = 100$, Prandtl number $Pr = 0.72$, $\gamma = 1.4$. 100 grid points are used in the wall normal direction.

4.1 2-D PSE results at Mach 1.5

The linear stability characteristics for Mach 1.5 flat plate boundary layer were studied using PSE with a single domain spectral collocation method in some detail by Bertolotti [8]. We use this case as a benchmark case for code validation and method evaluation. The stagnation temperature is $T_0 = 298.58K$. The frequency F defined as

$$F = \frac{2\pi f\nu}{U_\infty^2} \quad (55)$$

is $F = 40 \times 10^{-6}$. ϵ is set to 10^{-9} in updating α. The initial conditions come from the nonparallel LST solutions. Figure 4 shows the growth rate based on parallel LST and PSE formulations using u and E normalization formulas. The parallel linear stability and PSE

results from Bertolotti [8] are also shown for comparison purposes. The parallel linear stability results are seen to be in good agreement. The PSE results using u normalization agree quite well in general. The disagreement at low Reynolds number may be contributed to different marching step size and maybe different initial conditions. Another feature to be noticed is the different growth rates result from different normalization formulas (u and E formulas in this case). This feature makes the nonparallel effects hard to interpret because the growth rate based on u is generally smaller than that based on E, while the parallel stability results are in between at Reynolds number less than 800. The real part of the wavenumbers from LST and PSE using u and E normalization formulas are shown in the bottom plate of Fig. 4. It is quite interesting to notice that although the two normalization formulas produce quite different growth rate curves, which envelope the parallel LST results at $R < 800$, their real wavenumbers α_r are close and are quite different from their LST counterparts. Indeed, although different growth rate curves are produced by using different normalizations, the recombined instant disturbances $\hat{q}e^{-\alpha_i}(cos\alpha_r, isin\alpha_r)$ prove to be the same. This is shown in Fig.5 for both $\tilde{u}_r$ (top plate) and $\tilde{p}_r$ (bottom plate) in contours over the disturbance field. The results using different normalization formulas produce the same contours. This fact can serve as a check for the various normalizations in that different normalizations should return the same instantaneous disturbances.

The effects of using 4FDM and spectral collocation schemes for wall normal direction differentiations are illustrated in Fig.6. The growth rates α_i obtained using the two schemes are compared in the upper figure, the real wavenumber α_r the lower figure. The α_i comparisons show the difference to be within $O(1/R)$. The difference in α_r seems to be quite small. The choice of discretization schemes indeed depends on whether the schemes can provide proper cluster of grid points at regions of high gradient. In a low Mach number range, for example, at Mach 1.5, both schemes provide proper stretching. The situation changes as Mach number increases and the high gradient region moves outward from the wall. The use of the simple spectral collocation methods often fails to provide good results. The remedy may be the use of double domain spectral collocation methods, or high order finite difference schemes such as 4FDM with a stretching function clustering enough points in the middle region between the wall and the free stream. However, whether the convergent results can be obtained also depends on the streamwise marching step size as well as the the initial conditions.

In an attempt to resolve the issue whether the small difference in α_i from the PSE results as shown in Fig. 4 is due to the methods in obtaining initial conditions. The iterative Taylor expansion method described in Bertolotti [8] is implemented and used to obtain the initial conditions. These initial conditions and the nonparallel LST initial conditions as used to obtain two sets of PSE results which are compared in Fig. 7. It is evident that the use of different sets of initial conditions at Mach 1.5 does not affect the PSE results except near the starting position R_0.

The accuracy of PSE is known to be $O(1/R)$. The effects of different step sizes and different numbers of wall normal grid points are shown in Tables 1 and 2. The difference in α_i in both tables are well within $O(1/R)$, which indicates that the computational demand of PSE is quite flexible. We notice that using $N_y = 181$ as in the case shown in Table 2 does not lead to convergent results, which may be the result of high x and y step size ratio.

4.2   PSE results at other Mach numbers

Having studied the stability of Mach 1.5 flat plate boundary layer, the performance of the 2-D PSE code at other Mach numbers are explored. At Mach 0.02 and otherwise the same conditions as in the Mach 1.5 case, the parallel LST results and PSE results are shown in Fig. 8 in comparison with Bertolotti's results. The agreement is excellent. Also noticable is that the nonparallel effects, or the difference between the LST and PSE results, are quite small at this low Mach number.

Mach 1.6 results are shown in Fig. 9 for $b = 0$ (2-D wave) and $b = 0.1$ (oblique wave) cases, where $b = \beta R/1000$. The PSE results from Bertolotti is also shown. The results indicate that the instability is of first mode nature in that the instability is amplified when it is oblique. The other reason to show this comparison is the availability of PSE shape functions for the oblique wave case at $R = 750$ from Bertolotti [8]. The match in shape functions $|\hat{u}|$ and $|\hat{T}|$ shown in Fig.10 are excellent.

The Mach 4.5 results with $F = 120 \times 10^{-6}$ and $T_0 = 311K$ are shown in Fig. 11. 4FDM with a stretching function clustering grid points near a middle point outperforms the single domain collocation method with algebraic stretching. Both LST and PSE results are shown with Chang et al's results. [16] The first modes switch to second modes between $R = 1200$ and $R = 1400$. The nonparallel basic flow stablizes the first modes and destablizes the second modes.

4.3 3-D PSE results

The 3-D PSE code is implemented for solving the stability of hypersonic flow over 3-D elliptical cones. The results presented here are only a test case where the oblique disturbances of Mach 1.5 flow over a flat plate are simulated. 2-D PSE can handle this problem by simply setting a constant β and marching along a streamwise path. This test case serves as a test of concept, doability and correctness of the numerical codes for 3-D PSE. 3-D PSE use spanwise Fourier collocation differentiations to resolve the spanwise periodic wave components. 4 points are enough in the spanwise direction for the test runs. The initial conditions are the 3-D nonparallel linear stability results expanded in z direction by multiplying linear stability eigenfunctions with $e^{i\beta z}$. For the current numerical setup, the inversion of the complex square matrix of rank $5 \times 100 \times 4$ is needed and is the most costly computational task. Figure 12 shows the growth rates by the 2-D and 3-D PSE methods as well as the results from Bertolotti. [8]. The 2-D and 3-D PSE results are found to be identical up to machine precision. Finally, the 3-D disturbance field obtained with the 3-D PSE are shown in Fig.13 in contours of $\bar{p}_r$ (upper figure) and $\bar{u}_r$ (lower figure). The oblique wave angle and the growth of the 3-D disturbances are clearly illustrated.

5 Conclusions

2-D and 3-D PSE codes are developed and tested for the stability of supersonic flow over flat plate cases. Numerical aspects of PSE are discussed including the effects of different discritization schemes, different initial conditions. The effects of nonparallel basic flow are also discussed. The 3-D PSE procedures are laid out and will be used to solve for the stability of hypersonic flow over an elliptical cone case.

6 Acknowledgements

References

[1] L. Lees and C. C. Lin. Investigation of the stability of the laminar boundary layer in a compressible fluid. *NACA Tech. Note 1115*, 1993.

[2] L. M. Mack. Boundary-layer linear stability theory. *AGARD Rep. 704,3-1*, 1984.

[3] A. R. Wazzan, T. T. Okamura, and A. M. O. Smith. Spatial and temporal stability charts for the falkner-skan boundary layer profiles. *McDonnell-Douglas Aircraft Co., Rept. No. DAC-67086*, 1968.

[4] M. R. Malik and S. A. Orzag. Efficient computation of the stability of three-dimensional compressible boundary layers. *AIAA Rep. No. 81-1277*, 1981.

[5] X Zhong. Direct numerical simulation of hypersonic boundary layer transition over blunt leading edges, part i: A new numerical method and validation. *AIAA-97-0755*, 1997.

[6] X Zhong. Direct numerical simulation of hypersonic boundary layer transition over blunt leading edges, part ii: Receptivity to sound. *AIAA-97-0756*, 1997.

[7] X. Zhong and H. Dong. Hypersonic boundary layer receptivity to freestream disturbances over elliptic cross section cone. *AIAA-99-0409*, 1999.

[8] F. P. Bertolotti. Compressible boundary layer stability analyzed with the pse equations. *AIAA-91-1637-CP*, 1991.

[9] F. P. Bertolotti, Th. Herbert, and P. R. Spalart. Linear and nonlinear stability of the blasius boundary layer. *J. Fluid Mech.,vol 242;441-74*, 1992.

[10] Th. Herbert. Parabolized stability equations. *AGARD Rep. No.793*, 1994.

[11] Th. Herbert. Parabolized stability equations. *Annu. Rev. Fluid Mech.*, 29:245–283, 1997.

[12] H. Haj-Hariri. Characteristics analysis of the parabolized stability equations. *Studies in Applied Mathmatics, vol 92; 41-53*, 1994.

[13] F. Li and M.R. Malik. Mathematical nature of parabolized stability equations. *in Laminar-Turbulent Transition*, 1994.

[14] C. L. Chang, M. R. Malik, G. Erlebacher, and M. Y. Hussaini. Compressible stability of growing boundary layers using parabolized stability equations. *AIAA-91-1636*, 1991.

[15] C. Airiau and G. Casalis. Nonlinear pse compared with dns and experiment. *in Laminar-Turbulent Transition, pp.85-92*, 1994.

[16] C. L. Chang and M. R. Malik. Non-parallel sta-
bility of compressible boundary layers. *AIAA-93-
2912*, 1993.

[17] C.L. Chang and M. R. Malik. Oblique-mode
breakdown and secondary instability in supersonic
boundary layer. *J. Fluid Mech.,vol 273, 323-360*,
1994.

[18] C. L. Chang, H. Vinh, and M. R. Malik. Hyper-
sonic boundary-layer stability with chemical reac-
tions using pse. *AIAA-97-2012*, 1997.

[19] Herbert Th. Progress in applied transition analy-
sis. *AIAA Paper 96-1993*, 1996.

[20] Herbert Th. On the stability of 3d boundary lay-
ers. *AIAA Paper 97-1961*, 1997.

[21] S. H. Hu and X. Zhong. Hypersonic boundary-
layer stability over blunt leading edges with bow-
shock effects. *AIAA-98-0433*, 1998.

[22] M. R. Malik. Numerical methods for hypersonic
boundary layer stability. *Journal of Computa-
tional Physics*, 86:376–413, 1990.
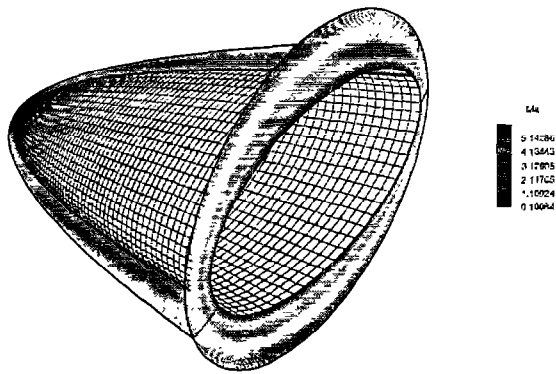
Figure 1: Mach 15 flow over a 2:1 blunt elliptical body The cross section contours are the Mach number con tours.
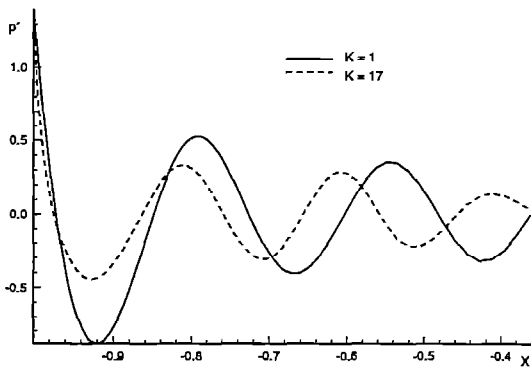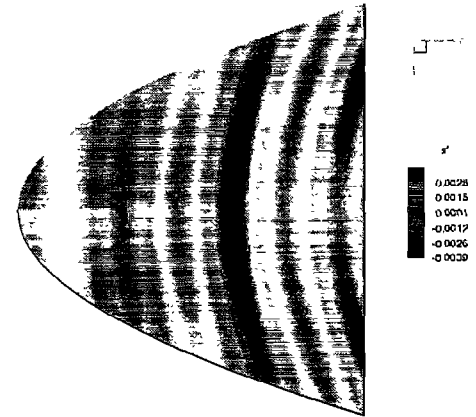
Figure 2: Instantaneous presure perturbations on body surface induced by freestream plannar acoutstic disturbances on two spanwise locations.
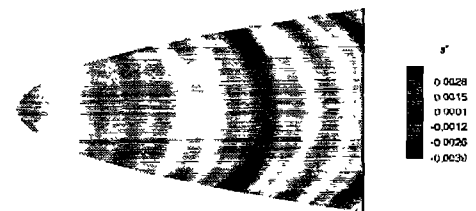
Figure 3: Mach 15 flow unsteady receptivity simulation results. Instantaneous entropy perturbations on body surface induced by freestream plannar acoutstic disturbances.
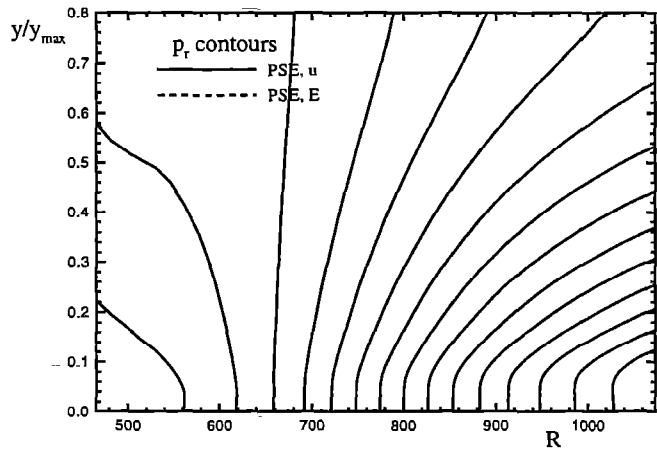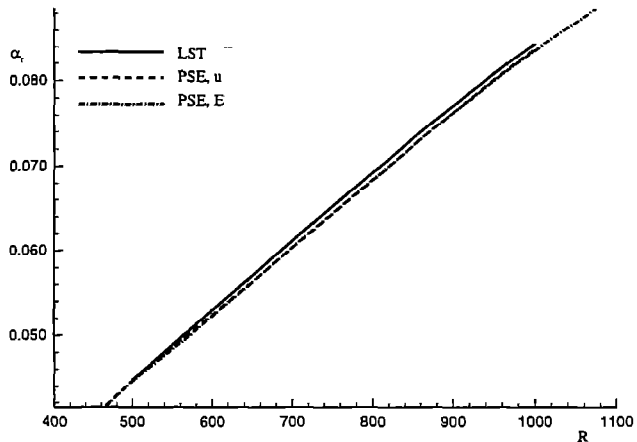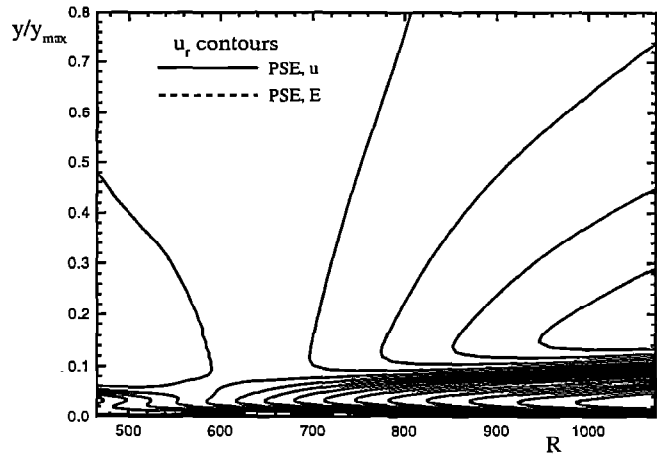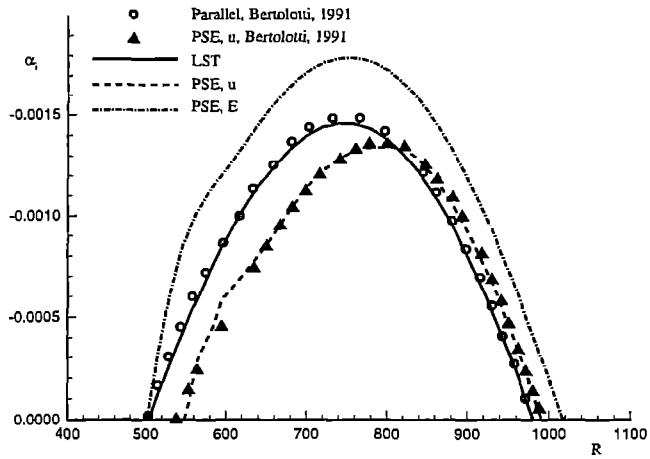
Figure 4: Linear stability results at Mach 1.5. Growth rate, α_i, is shown in the top plate. Wavenumber, α_r, is shown in the bottom figure. Parallel linear stability results are compared with the nonparallel PSE results using u and E normalization formulas. In the top plate, results from Bertolotti (1991) is also shown for comparison.

Figure 5: Instantaneous disturbance contours. The shape functions and the complex wavenumbers (α_r, α_i) are recombined to give the disturbances. Top half, $\tilde{u}_r$, bottom half, $\tilde{p}_r$.

Figure 7: Nonparallel PSE results at Mach 1.5. Results using initial conditions obtained from nonparallel LST solutions and from the iterative Taylor expansion methods are compared along with Bertolotti's results (1991).
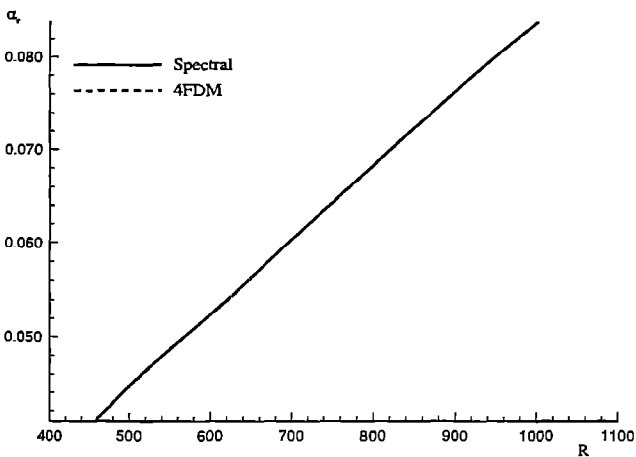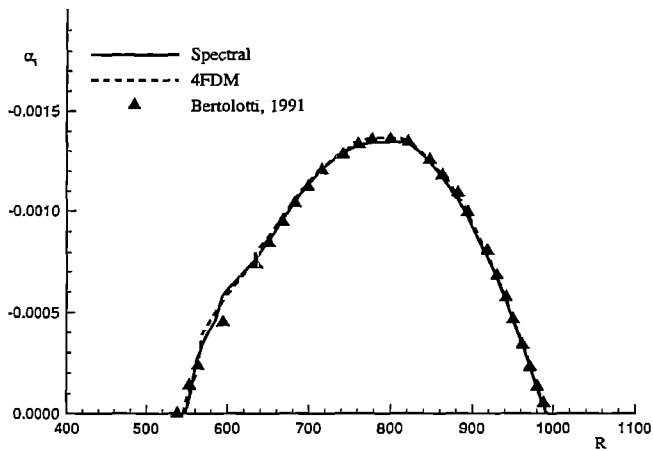
Figure 6: Linear stability results at Mach 1.5. Growth rate, α_i, is shown in the top plate. Wavenumber, α_r, is shown in the bottom figure. Nonparallel PSE results using 4FDM and spectral collocation methods are compared.
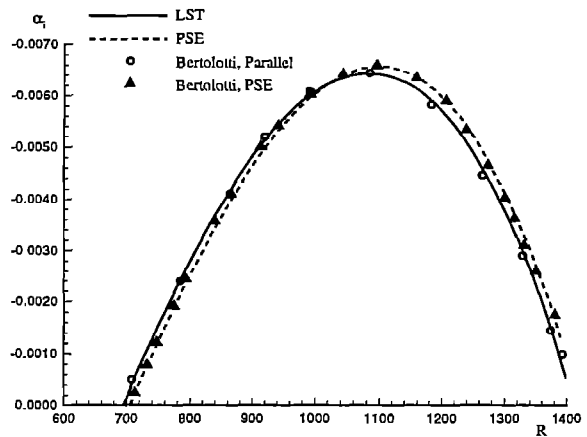
Figure 8: Growth rates at Mach 0.02. Parallel linear stability results are compared with the nonparallel PSE results using u normalization formulas. Results from Bertolotti (1991) is also shown for comparison.

13

Disturbance profiles
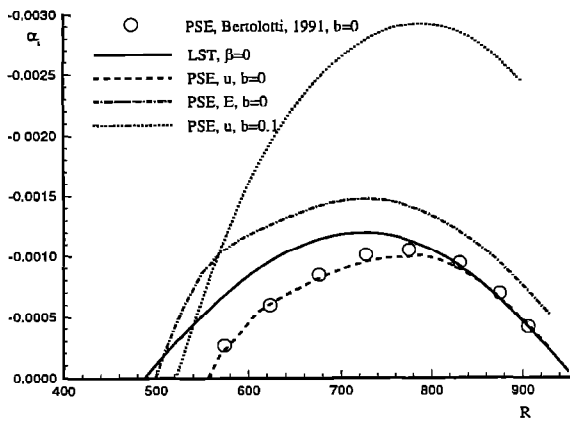
Figure 9: Growth rates at Mach 1.6 for $b = 0$ and $b = 0.1$. For $b = 0$, parallel linear stability results are compared with the nonparallel PSE results using u and E normalization formulas. Results from Bertolotti (1991) is also shown for comparison. For $b = 0.1$, only the u normalization results are shown.

Disturbance profiles
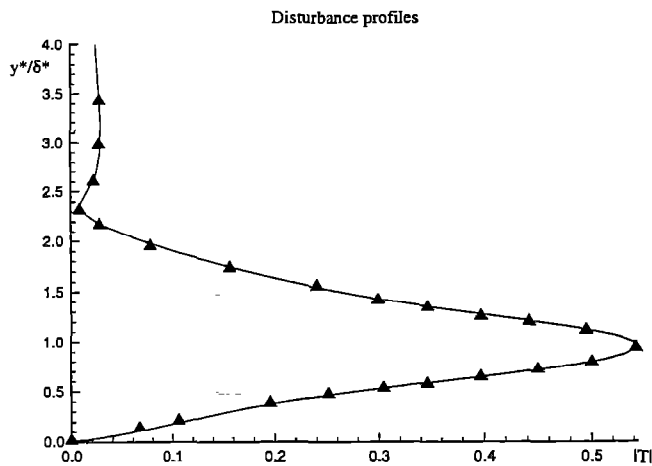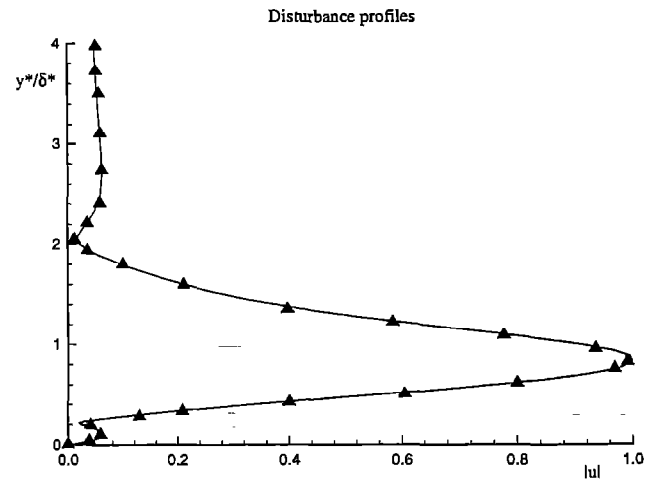
Figure 10: PSE shape functions $|\hat{u}|$ (upper plate) and $|\hat{T}|$ (lower plate) at Mach 1.6 with $b = 0.1$. The symbols are results from Bertolotti (1991).

14
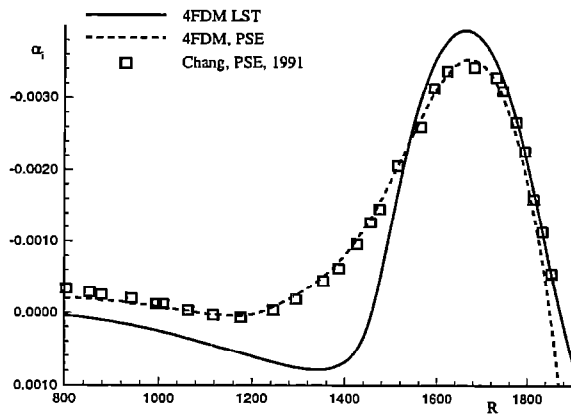
Figure 11: Growth rates at Mach 4.5. Parallel linear stability results are compared with the nonparallel PSE results using u normalization formula. Results from Chang (1993) is also shown for comparison.
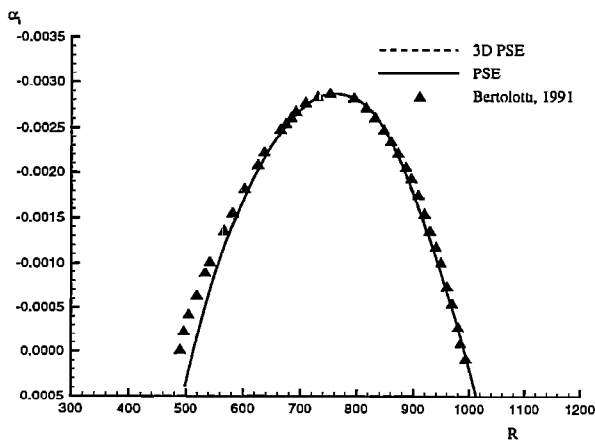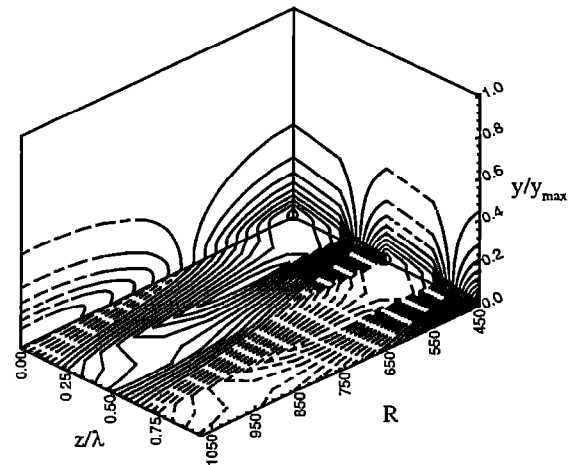
Figure 12: Comparisons of 2-D and 3-D PSE results at Mach 1.5 for $b = 0.15$. Growth rates are updated using u normalization formula. Results from Bertolotti (1991) is also shown for comparison.
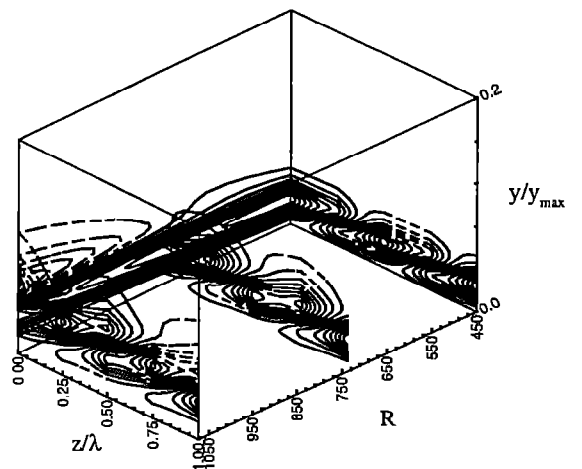
Figure 13: 3-D PSE results at Mach 1.5 for $b = 0.15$. Upper figure, contours of $\tilde{p}_r$. Lower figure, contours of $\tilde{u}_r$.